

Effect of Cyclic Stress on Corrosion Behavior of 7A09 Aluminum Alloy in Tropical Coastal Atmosphere

Laizheng Luo^{1,3}, Bin Wang^{2,*}, Jie Zhou², Jie Liu⁴, Xiaohui Wang¹

¹ Southwest Technology and Engineering Research Institute, Chongqing Engineering Research Center for Environmental Corrosion and Protection, Chongqing, 400039, China

² School of Chemistry and Materials Science, Ludong University, Yantai, 264025, China

³ College of Chemistry & Chemical Engineering, Chongqing University, Chongqing, 400039, China

⁴ College of Chemistry and Chemical Engineering, Yantai University, Yantai, 264005, China

*E-mail: wb7411@163.com

Received: 11 September 2022 / Accepted: 15 October 2022 / Published: 17 November 2022

In order to simulate the actual service conditions of the structural materials used in the superstructure of marine equipment, the tropical coastal atmosphere was used as the corrosion environment of thin electrolyte layer for 7A09 alloy in this work, and the specifically designed outdoor device was utilized to apply the elastic cyclic stress. Then the corrosion behavior of 7A09 alloy under the combined effects of atmospheric corrosion of thin electrolyte layer and elastic cyclic stress was investigated. The results indicate that the elastic cyclic stress can accelerate the corrosion process of 7A09 alloy significantly under the test conditions, and which contributes more to the increase in the cathodic reaction. The applied stress has a greater effect on the degradation of mechanical properties than on the corrosion morphology. In addition, the interaction mechanism between atmospheric corrosion of thin electrolyte layer and elastic cyclic stress was also discussed.

Keywords: atmospheric corrosion; thin electrolyte layer; elastic cyclic stress; 7A09 alloy; interaction mechanism

1. INTRODUCTION

As an ideal structural material in engineering applications, the aluminum alloys are extensively used in the superstructure of marine equipment due to their excellent combination of properties including favorable strength-to-weight property, thermal conductivity and fracture toughness [1,2]. As the service environment of the superstructure of marine equipment, the marine atmosphere presents the characteristics of high humidity, high temperature and high salt spray, and which will form a thin electrolyte layer on the surface of aluminum alloy structural materials [3]. Thus atmospheric corrosion of thin electrolyte layer will occur in the presence of corrosion medium such as chloride ions, sulfur

dioxide and oxygen. At the same time, the marine equipments serving in ocean are usually subjected to dynamic stresses like waves, currents, winds and working stress. It is noteworthy that most of the stresses should be in the elastic range and have the characteristics of randomness, cyclicity and complexity. Thus, under the actual service conditions, the aluminum alloy structural materials used in the superstructure of marine equipment endure the combined effects of atmospheric corrosion of thin electrolyte layer and elastic cyclic stress. The interactions between them enhance corrosion reactions, leading to accelerated failure of structural materials [4]. Despite this, there is very little information on this subject, and the intrinsic interactions between them still remain unclear.

Some researchers have studied the effects of elastic stress on the electrochemical corrosion of steels, but the results of which are somewhat confusing. It has been assumed that the free energy increment caused by elastic deformation is insufficient and the effect of tensile stress in the elastic regime on corrosion of steels is unapparent [5, 6]. Xu et al.[7] also reported that the static elastic stress showed no effect on the corrosion potential of X100 pipeline steel in a near-neutral pH solution. However, many researchers hold the opposite points [4,8-12], they have found that elastic stress could result in negative shift of corrosion potential and accelerate corrosion rates of steels significantly. In addition, the linear relationship between corrosion potential and external stress has also been proven by some workers [13,14]. However, until now, the vast majority of existing studies have been restricted to laboratory experiments and which are conducted in well-controlled electrolytes using immersion tests. As mentioned above, the aluminum alloy structural materials used in the superstructure of marine equipment suffer atmospheric corrosion caused by a thin electrolyte layer on the surface. The mass transfer process, hydration of dissolved metal ions and accumulation of corrosion products under such a thin electrolyte layer on the surface are very different from those of an immersion in an electrolyte. Additionally, the corrosion factors of structural materials in the two environments are also fundamentally different. Climatic factors including relative humidity, solar radiation, time of wetness, changes in temperature, wind speed, together with other contaminants, are main contributors to outdoor atmospheric corrosion [15]. On the other hand, most of the research has been conducted under constant loads, however, in the actual situation, marine structures serving in ocean are usually subjected to dynamic loads [16]. Therefore, it is an urgent issue to conduct a research on the corrosion behavior of aluminum alloy structural materials under the combined effects of atmospheric corrosion of thin electrolyte layer and elastic cyclic stress.

In this study, the outdoor marine atmosphere was used as the corrosion environment of thin electrolyte layer for 7A09 aluminum alloy, and the outdoor device which was specifically designed by Southwest Technology and Engineering Research Institute was utilized to apply the elastic cyclic stress. Then the corrosion behavior of 7A09 alloy was investigated under the combined effects of atmospheric corrosion of thin electrolyte layer and elastic cyclic stress, and the interaction mechanism of which was also discussed. The results obtained by this case study may provide an essential insight into the effects of elastic cyclic stress on the atmospheric corrosion process of actual marine structures.

2. EXPERIMENTAL PROCEDURES

2.1 Material preparation

The material used in this work was 7A09 aluminum alloy in T6 temper which contains (in mass%): 5.80 Zn, 2.80 Mg, 1.49 Cu, 0.45 Fe, 0.23 Cr, 0.06 Si, 0.02 Ti, and Al to balance. The tensile strength and yield strength of the material used are 608 and 547 MPa, separately. Tensile samples were cut along the rolling direction, ground by silicon carbide abrasive papers to grit 2000 and then washed with ethanol.

2.2 Field exposure test

The natural exposure test was conducted in Wanning test site (18°58'N, 110°30'E) characterized by a tropical coastal atmosphere. As shown in Table 1, this test site has high levels of chlorine ion concentration and humidity. In addition, the self-designed homemade testing machine was adopted to apply the elastic cyclic stress on specimens, as shown in Fig.1 (a).

Table 1. Annual environmental data of the Wanning test site

Site	Mean temperature (°C)	Mean relative humidity (%)	Cl ⁻ (mg m ⁻² d ⁻¹)	SO ₂ (mg m ⁻² d ⁻¹)	pH of rain
Wanning	25.7	86	308	4.51	5.23



Figure 1. The self-designed homemade testing machine for stressed samples (a); the exposure frames for unstressed samples (b)

A sinusoidal stress waveform was employed to the specimen with a frequency of 10 Hz. The stress ratio of the cyclic stress was 0.1 and the maximum stress was 40% of the yield stress. Under such test conditions, the samples were subjected to elastic deformation in a tension-tension mode. The cyclic stress was applied once per day for 25 minutes. For comparison, all unstressed samples were mounted on exposure frames with a 45 degree angle to the horizontal line and placed facing south, as shown in Fig.1 (b).

2.3 Electrochemical measurement

The electrochemical properties of the samples after different exposure times were conducted on a CHI660E electrochemical workstation in a 3.5% NaCl solution with platinum sheet as the counter electrode and a saturated calomel electrode (SCE) as the reference electrode. The polarization curve tests were performed in the potential range of +300 mV to -300 mV versus the open-circuit potential at a sweep rate of 0.5 mV/s. The EIS measurements were carried out in the frequency range between 10 mHz to 100 kHz using a perturbation amplitude of 10 mV at the open-circuit potential.

2.4 Characterization of corrosion morphology and corrosion products

The JEOL JSM-820 scanning electron microscope and energy dispersive spectroscopy (EDS) were used to characterize the corrosion product layer on the surface and its element distributions, separately. After removing the corrosion products in a solution (1 L H₂O + 20 g CrO₃ + 50 mL H₃PO₄) at 80°C for 6 minutes, the corrosion morphologies of the samples were observed in metallographic cross sections by optical microscopy.

2.5 Mechanical properties measurement

The mechanical properties of the specimens were investigated on MTS-810 tensile testing machine based on ASTM E8M specification with a deformation rate of 1mm/min in air at room temperature.

3. RESULTS AND DISCUSSION

3.1 Microstructure examination

Fig.2 displays the typical microstructure of 7A09-T6 alloy. It is observed that the microstructure of this alloy presents the characteristic of some irregularly shaped intermetallic particles with an inhomogeneous distribution. The typical constituents of these intermetallic particles of the studied alloy have been identified to be Mg(ZnAlCu)₂, Al₂CuMg, Mg₂Si and FeAl₃ [17,18]. Due to the existence of these intermetallic precipitates, the native oxide film formed on the surface of the

specimen will be defective and inhomogeneous, and which could be preferentially attacked by corrosive medium, leading to the occurrence of pitting corrosion.

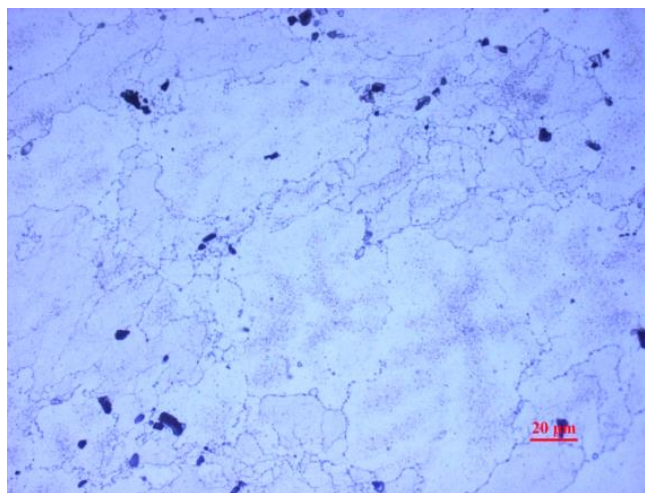


Figure 2. Microstructure of 7A09-T6 aluminum alloy

3.2 Electrochemical measurement results

3.2.1 Potentiodynamic polarization curves

Fig.3 shows a comparison of polarization curves of the studied samples under different test conditions. The anodic curves of all the samples with stress and without stress display similar corrosion behavior, neither of the samples shows passivation region, suggesting that active dissolution takes place. A similar phenomenon has been observed by Shen et al. [19]. They have found that cyclic stress can promote the process of anodic dissolution but does not affect the mechanism of anodic reaction. The rapid increase in anodic current densities with potential indicates that the values of pitting potential E_{pit} and corrosion potential E_{corr} are very close and the samples suffer from pitting corrosion at the E_{corr} [20]. On the other hand, the cathodic branches of all the tested samples show a limited current region, which indicates that the corrosion processes of all the tested samples are under cathodic control (oxygen diffusion).

The parameters of corrosion current density (I_{corr}) obtained by the Tafel extrapolation method as well as corrosion potential (E_{corr}) are listed in Table 2. Observing the change law of E_{corr} , it can be seen that the E_{corr} values for both the stressed and unstressed samples remain relatively stable with the prolongation of exposure time. However, when the elastic cyclic stress applies, the E_{corr} values become more negative, suggesting that the surfaces of the stressed samples become more active. The I_{corr} values of the specimens under both test conditions all increase with exposure time, indicating the increase in corrosion rates with increasing time. In addition, it is evident from Fig.3 that the applied stress results in higher anodic and cathodic reaction rates of the alloys compared with the curves of the unstressed specimens, leading to a significant increase in the corrosion current density. As listed in

Table 2, the I_{corr} value of the stressed specimen exposed for 35 days is approximately two times higher than that of the unstressed specimen exposed for 6 months. Especially, it can also be observed from Figure 3 that the applied stress can contribute more to the increase in the cathodic reaction than the anodic dissolution reaction. The similar conclusion has been drawn by Kim from his study of the effect of elastic tensile stress on the electrochemical corrosion behavior of ferritic steel in a sour environment [21].

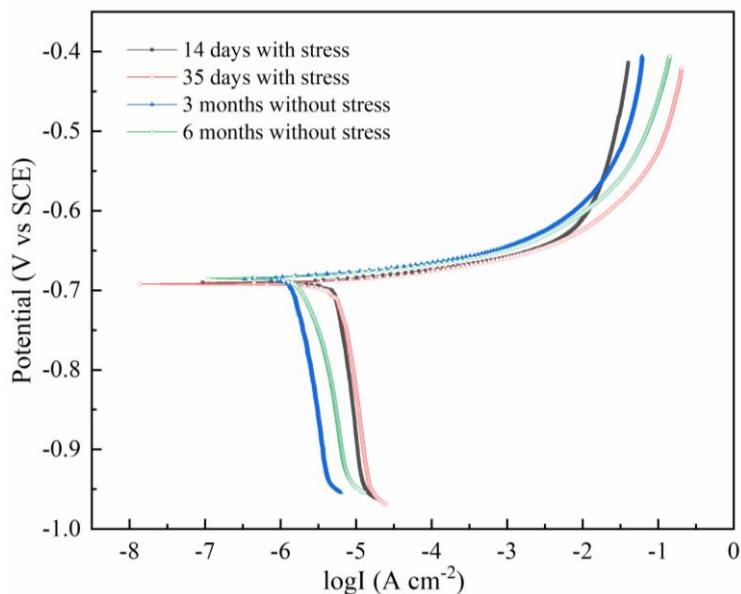


Figure 3. Potentiodynamic polarization curves of the examined specimens with corrosion products after different exposure times

Table 2. Polarization curve parameters of 7A09 alloys under different test conditions

Samples	Corrosion potential E_{corr} (V vs SCE)	Corrosion current density I_{corr} ($\mu\text{A cm}^{-2}$)
14 days with stress	-0.692	5.302
35 days with stress	-0.694	6.574
3 months without stress	-0.684	1.642
6 months without stress	-0.683	2.606

3.2.2 EIS measurement

Fig.4 exhibits the EIS plots of 7A09 alloys under various test conditions over different exposure times. By reading the Nyquist plots, the shapes of all the curves for both the stressed and unstressed samples are similar, which present a depressed capacitive loop in high frequency range and an inductive loop in low frequency range. The presence of inductive loop has been reported to be related to pitting processes [22,23]. When pitting corrosion occurs, corrosion products are formed on

the surfaces of 7A09 samples, and which has a certain protective effect against further corrosion attacks. However, the resistance of the corrosion product layer is usually much smaller than the charge transfer resistance, thus as shown in Fig.4 (b), wide phase angle peaks at high frequency ranges are observed in the Bode plots, and the valleys at low frequency ranges are assigned to the inductive loops in the Nyquist plots. Thus, the electric equivalent circuit in Fig.5 is employed for fitting the EIS data, in which R_s corresponds to the electrolyte resistance, CPE_{dl} as well as CPE_f describe the capacitance behaviors of the double layer and corrosion product layer, respectively. R_{ct} and R_f are adopted to illustrate the charge transfer resistance and the resistance of corrosion product layer, separately. L and R_L stand for the inductance element and its resistance, respectively. The solid lines in Fig.4 are fitting results, which show a very high fit of experimental data to the employed equivalent circuit. In order to fit EIS data more accurately, the constant phase element (CPE) is used to replace the ideal capacitor. The impedance (Z) and the capacitance (C) of the CPE are defined as below [24]:

$$Z = Y^{-1} (j\omega)^{-n} \tag{1}$$

$$C = Y^{1/n} R^{(1-n)/n} \tag{2}$$

where n and Y stand for the CPE exponent and CPE constant, respectively. j describes the imaginary component and ω represents the angular frequency in rad s^{-1} .

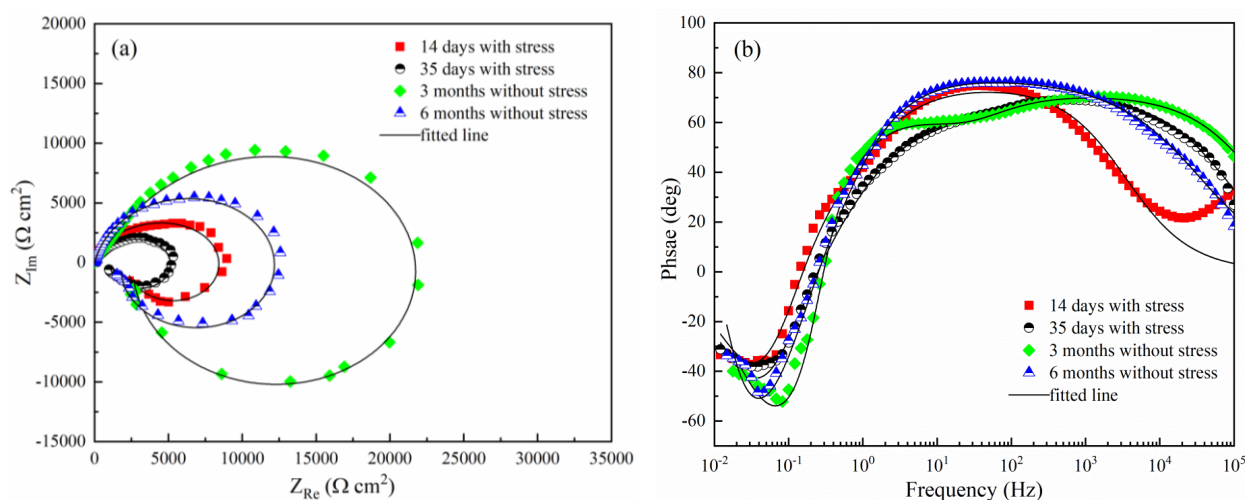


Figure 4. EIS of 7A09-T6 alloys after different exposure times in a tropical coastal atmosphere with and without stress loaded (a) Nyquist plots; (b) Bode plots

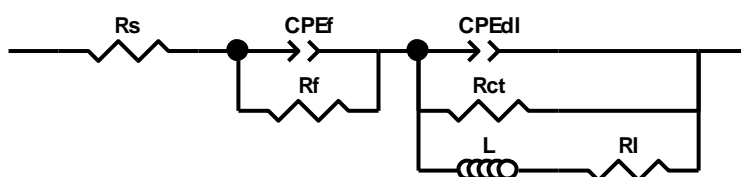


Figure 5. The equivalent circuit model used for fitting the EIS data

The results of EIS fitting are listed in Table 3, among which the definition of C_{dl} and C_f can be obtained by equations (3) and (4) based on the plate capacitor model:

$$C_{dl} = \frac{\varepsilon \varepsilon_0 A_{dl}}{d_{dl}} \quad (3)$$

$$C_f = \frac{\varepsilon \varepsilon_0 A_f}{d_f} \quad (4)$$

where ε and ε_0 correspond to the relative static permittivity and the electric constant, separately. A_{dl} and A_f characterize the area at which the charge transfer process occurred and the effective area of corrosion product layer, respectively. Accordingly, d_{dl} and d_f stand for the thicknesses of the electrical double layer and the corrosion product layer, separately.

Table 3. Fitted results of EIS plots for 7A09 alloys under different test conditions

Samples	R_{ct} ($k\Omega \text{ cm}^2$)	R_f ($k\Omega \text{ cm}^2$)	C_{dl} ($\mu\text{F cm}^{-2}$)	C_f ($\mu\text{F cm}^{-2}$)
14 days with stress	8.972	0.117	34.03	7.97
35 days with stress	5.500	0.273	43.76	11.02
3 months without stress	30.320	0.456	18.86	35.91
6 months without stress	12.940	1.550	19.48	69.30

Since the R_{ct} value is inversely proportional to the corrosion rate of metals, so the corrosion rate can be characterized by the parameter of R_{ct} . It can be inferred from the R_{ct} values in Table 3 that the corrosion rates for both test conditions increase significantly with exposure time, which is in accordance with the results obtained by polarization curves. It is also evident that the R_{ct} values of the stressed samples are far smaller than those of unstressed ones, indicating that the applied stress results in an increasing corrosion rate of 7A09 alloy, and which agrees with the results obtained by Han et al. [25]. They have demonstrated that the cyclic alternating load can significantly accelerate the corrosion process of magnesium alloys in the Hank's balanced salt solution.

The value of R_f can be used to reflect the protectiveness of corrosion product layer. The R_f values of specimens under each test condition increase slightly with exposure time due to the more corrosion products formed on the sample surfaces. However, the applied stress could lead to the increase in porous structure of corrosion products, and which will finally result in the formation of cracks on the corrosion product layer. Just as shown in Fig.6, compared with the corrosion product layer formed on the sample surface under unstressed condition, the corrosion product layer of the specimen under dynamic stress condition is less compact and has many superficial cracks on it, and the similar phenomenon have also been observed by other researchers [25,26]. Besides, with the function of cyclic alternating stress, this corrosion product layer is more likely to be broken and split of the surface, leading to the decrease in A_f and the increase in A_{dl} , and which is also the reason why the C_{dl} values of the stressed samples are higher and the C_f values are lower than those of the unstressed

ones. Consequently, based on the characteristics of the corrosion products formed on the surface of the stressed samples as described above, this corrosion product layer cannot effectively offer the protective effect on the corrosion of the alloy, and this is also the main reason why the R_f and R_{ct} values of the specimens with stress are much smaller than those of the specimens without stress, just as listed in Table 3.

In addition to the differences in the surface morphologies and properties of the corrosion products of the stressed and unstressed specimens, the applied stress could also introduce strain energy to the alloy and leads to the formation of local deformation and then more dislocations in the alloy, which will consequently enhance the activity of the alloy [27,28], therefore, the alloy is more susceptible to corrosion attack. Once corrosion such as pit generates, the applied stress could also play an important role in promoting further corrosion. The bottom of the pit is equivalent to the crack tip, and stress concentration phenomenon could occur at this local area, leading to the generation of plastic deformation even the stress is below yield strength. The effect of plastic strain becomes conspicuous at the bottom of pit, which results in rapid increase in anodic dissolution rate of the alloy and in turn contributes to further corrosion [5,29].

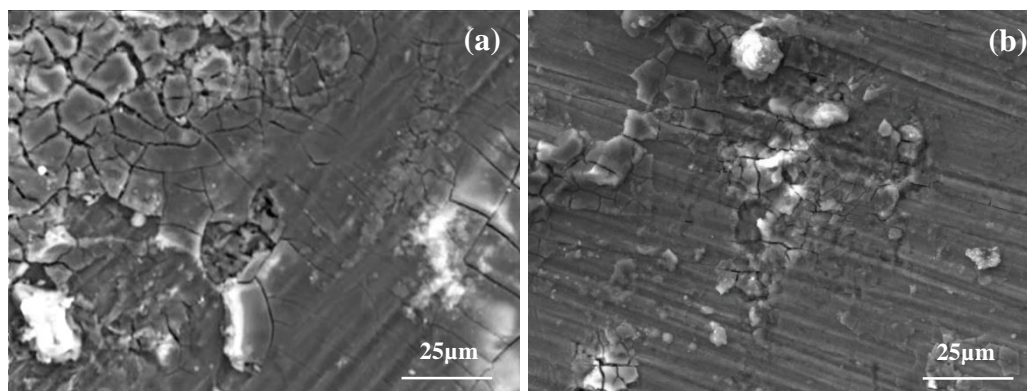


Figure 6. Surface morphologies of 7A09 samples after exposure in the tropical coastal atmosphere under different test conditions: (a) 35 days with stress; (b) 3 months without stress

3.3 Corrosion morphology

Cross-sectional morphologies of the studied samples were analysed using optical microscope. The stressed sample exposed for 14 days remains relatively intact and there are several discrete pits on the surface, and the maximum pitting depth is 19.9 μm . However, as displayed in Fig.7, all the other samples suffer from pitting corrosion as well as intergranular corrosion (IGC), and exfoliation corrosion is not observed. The maximum corrosion depth of the stressed sample exposed for 35 days is 48.7 μm , which is almost equal to that of the unstressed sample exposed for 3 months of 53.0 μm . The unstressed sample exposed for 6 months corrodes more severely. The corrosion area almost covers the entire surface, and the maximum corrosion depth reaches up to 85.0 μm .

It has been widely reported that intergranular corrosion (IGC) mainly results from the local galvanic corrosion between the grain matrix and the grain boundary precipitates and/or between the

grain matrix and the precipitate-free zone (PFZ) [30,31]. As to 7A09-T6 alloy, it has been studied [32] that the IGC of which results from both of the above cases, which is mainly caused by the preferential dissolutions of the PFZ and the grain boundary precipitates $Mg(ZnAlCu)_2$ along grain boundaries during the galvanic corrosion.

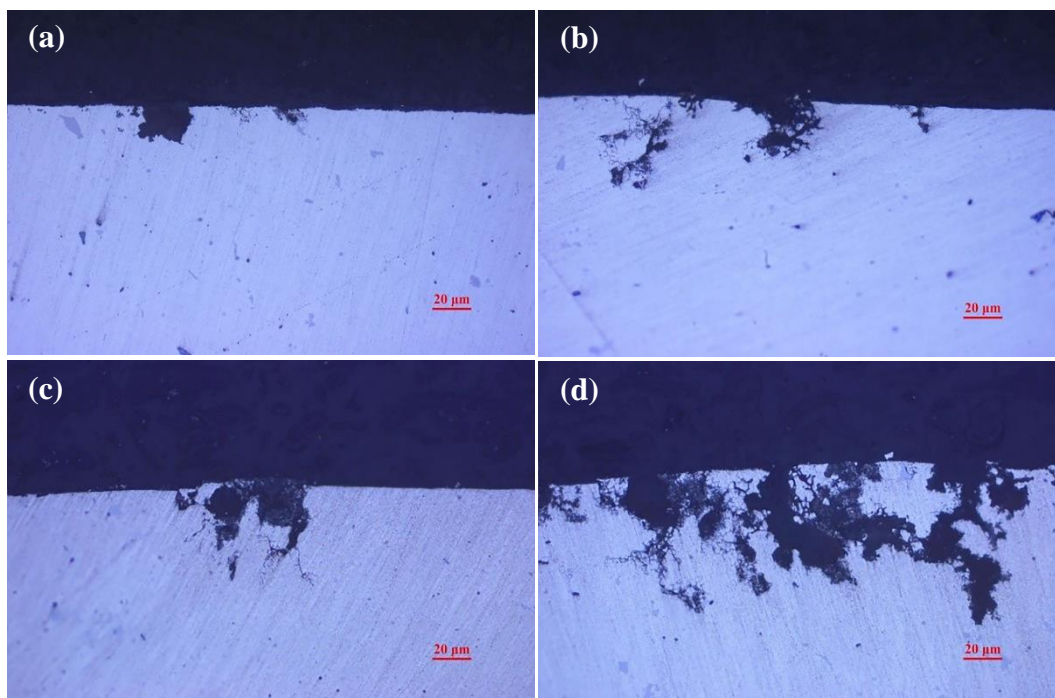


Figure 7. Cross-sectional morphologies of the samples after various exposure times under different test conditions: 14 days (a) and 35 days (b) of exposure with stress; 3 months (c) and 6 months (d) of exposure without stress

3.4 Loss in mechanical properties

Fig.8 shows the losses in mechanical properties of 7A09 specimens as a function of exposure time under various test conditions.

As to the unstressed samples, the mechanical property of tensile strength does not suffer obvious changes and the biggest loss of which is only 2.63% with exposure time of 12 months. However, for the case of elongation, the losses of which are much larger than those of tensile strength, and the biggest loss is 16.67%. With regard to the stressed samples, it can be clearly observed from Fig.8 that the applied stress significantly accelerates the deterioration of mechanical properties of the samples. The losses in tensile strength and elongation for the stressed samples with 35 days exposure are close to and larger than those of the unstressed samples with exposure time of 12 months, separately. In addition, the deterioration trend of mechanical properties of the stressed specimens is more obvious with exposure time than that of the unstressed specimens.

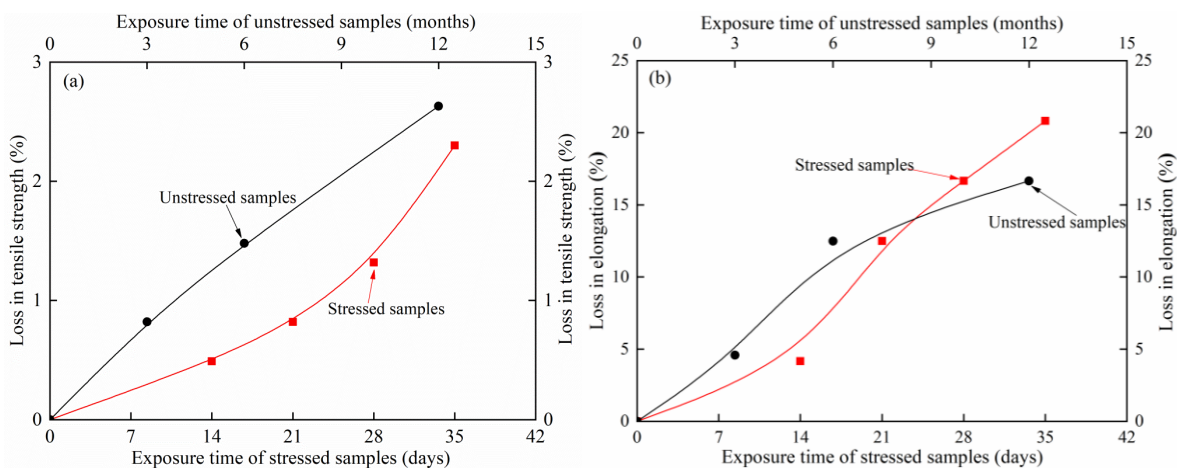


Figure 8. Losses in mechanical properties of stressed and unstressed 7A09 samples versus exposure time at the test site: (a) loss in tensile strength; (b) loss in elongation

3.5 Characterization of corrosion products

EDS plane scanning analysis was conducted to characterize the composition and distribution of elements of corrosion product of the stressed sample, and the results of which are demonstrated in Fig.9. The mass fractions of the main elements detected in Fig.9 (a) are as follow: Al 29.83%, O 42.46%, C 21.13%, Na 0.66%, Si 0.55%, Mg 0.50%, S 4.28%, Cl 0.59%. Among the main elements, the content of O and Al are relatively large, suggesting that the main composition of corrosion product is aluminum oxide. In addition, the presence of relatively high amount of C besides Al and O may be from carbonaceous pollutants like tarry aerosols and smoke, and which has been reported to have an enhancing effect on the corrosivity of atmospheric sulphur dioxide [33]. The Na and Si elements are probably introduced by dust particles in atmosphere. Mg is the element disclosed in the matrix.

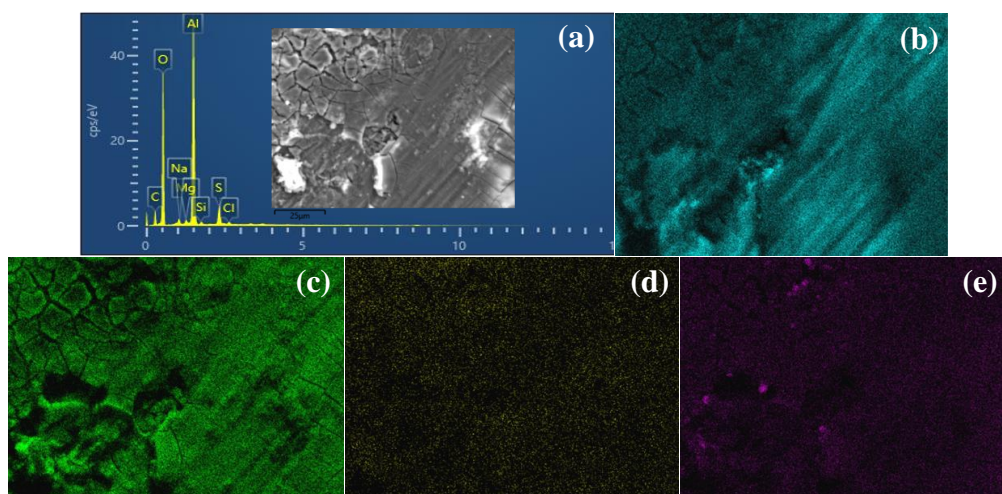


Figure 9. EDS results of the stressed 7A09 specimen after exposure for 35 days in the tropical coastal atmosphere. Energy spectrum diagram (a); Mapping of different elements: Al (b), O (c), Cl (d), S (e)

It can be seen from Fig.9 (d) that the element distribution of Cl on the surface is relatively uniform. Cl mainly comes from the gaseous HCl in atmosphere, rainwater or the deposition of sea salt. The Cl^- exhibits high mobility in aqueous solution and the ionic radius of which is very small. So Cl^- can penetrate the surface layer easily and can replace OH^- in $\text{Al}(\text{OH})_3$ step by step to form soluble aluminum chloride [15,34]. However, because of the washing of rainwater and the migration of Cl^- towards the bottom of corrosion pit, the content of chlorine containing species in outer corrosion product layer should be very small, and which is consistent with the results of EDS.

S is possibly from SO_4^{2-} in acid rain or SO_2 in atmosphere, as shown in Fig.9 (e), the element distribution of S on the surface is uneven. Under humid conditions, SO_2 can combine with H_2O to form sulfite (H_2SO_3), and which will finally be oxidized to H_2SO_4 by transition metal ions, ozone and hydrogen peroxide [35,36]. H_2SO_4 could react with the native oxide layer to form insoluble basic aluminum sulfates or amorphous aluminum sulfate hydrate [32].

4. CONCLUSIONS

The corrosion behavior of 7A09 alloy under the combined effects of atmospheric corrosion of thin electrolyte layer and elastic cyclic stress has been studied, and the following conclusions can be made:

(1) The 7A09 alloy suffers pitting corrosion and intergranular corrosion under the test conditions, and the corrosion rates of both stressed and unstressed samples all increase with exposure time.

(2) The elastic cyclic stress makes the alloy surface more active and accelerates the corrosion process of the alloy significantly, and which specially contributes more to the increase in the cathodic reaction than the anodic dissolution reaction.

(3) The applied stress reduces the protective effect of the corrosion products by increasing the porous structure and formation of cracks in the corrosion product layer. Besides, the applied stress could also play an important role in promoting further corrosion once pits generate.

(4) The applied stress has a greater effect on the degradation of mechanical properties of 7A09 alloy. The losses in mechanical properties for the stressed samples with 35 days exposure are close to and/or even larger than those of the unstressed samples after exposure for 12 months.

ACKNOWLEDGEMENTS

This work is supported by the National Natural Science Foundation of China (Grant Nos. 51901096 and 51971192), the Equipment Pre-research Field Fund (Grant No. 80904020507) and the National Defense Technology Foundation of China (HDH59030102).

References

1. H.S. Lai, X.W. Jiang, H.L. Li, H.Y. Cui, Z.L. Zhao, H. Guo and L. Li, *Int. J. Electrochem. Sci.*, 17(2022) 220559.
2. W.J. Wang. *Mater. Rep.*, 27(2013) 98.

3. Q.Y. Zhao, C. Guo, K.K. Niu, J.B. Zhao, Y.H. Huang and X.G. Li, *J. Mater. Res. Technol.*, 12 (2015) 1350.
4. S. Zhang, X.L. Pang, Y.B. Wang and K.W. Gao, *Corros. Sci.*, 75 (2013) 293.
5. B.T. Lu, J.L. Luo, P.R. Norton and H.Y. Ma, *Acta Mater.*, 57 (2009) 41.
6. G.T. Park, S.J. Kim, K.Y. Kim, NACE - International Corrosion Conference Series (2010), San Antonio, TX, USA.
7. L.Y. Xu and Y.F. Cheng, *Corros. Sci.*, 59 (2012) 103.
8. X.G. Feng, X.Y. Lu, Y. Zuo, N. Zhuang and D. Chen, *Corros. Sci.*, 103 (2016) 66.
9. X.H. Wang, X.H. Tang, L.W. Wang, C. Wang and Z.Z. Guo, *Int. J. Electrochem. Sci.*, 9 (2014) 4574.
10. X.H. Wang, X.H. Tang, L.W. Wang, C. Wang and W.Q. Zhou, *J. Nat. Gas Sci. Eng.*, 21 (2014) 474.
11. K. Gao, D. Li, X. Pang and S. Yang, *Corros. Sci.*, 52 (2010) 3428.
12. J.Q. Yang and Q.Q. Wang, *Int. J. Pres. Ves. Pip.*, 110 (2013) 72.
13. J.R. Wang, L.Q. Zhu, S.X. Rao, Z. Zhang and Q.P. Zhong, *J. Chin. Soc. Corros. Prot.*, 25 (2005) 226.
14. S.X. Rao, L.Q. Zhu, D. Li, Z. Zhang and Q.P. Zhong, *J. Chin. Soc. Corros. Prot.*, 27 (2007) 228.
15. B. Wang, L.W. Zhang, H. Jiang, X.B. Li and L.K. Xu, *Mater. Corro.*, 69 (2018) 1516.
16. Z.Y. Jia, Y. Yang, Z. He, H.B. Ma and F. Ji, *Appl. Ocean Res.*, 93 (2019) 101942.
17. M.G. Yan, B.C. Liu, J.G. Li, S.P. Wu, J. Hua and B.L. Xu, *China aeronautical materials handbook*, China Standard Press, (2001) Beijing, China.
18. Q. Chen, X.S. Xia, B.G. Yuan, D.Y. Shu and Z.D. Zhao, *Mater. Sci. Eng. A*, 588 (2013) 395.
19. Y. Chen, *The influence of the fluctuating stress to the SCC behavior of X80 pipeline steel in near neutral environments*, Xi'an Shiyou University, China, 2015.
20. S. Gudic, I. Smoljko and M. Kliskic, *J. Alloys Compd.*, 505 (2010) 54.
21. S.J. Kim, *Int. J. Hydrogen Energ.*, 42 (2017) 19367.
22. S. Gudic, J. Radosevic and M. Kliskic, *Electochim. Acta*, 47 (2002) 3009.
23. J. Ryl, K. Darowicki and P. Slepski, *Corros. Sci.*, 53 (2011) 1873.
24. Q. Yun, H. Wu, Z. Zhang, D.G. Li and P. Liang, *Int. J. Electrochem. Sci.*, 17 (2022) 22077.
25. L.Y. Han, Z.W. Zhang, J.W. Dai, X. Li, J. Bai, Z.H. Huang, C. Guo, F. Xue and C.L. Chu, *Bioact. Mater.*, 7 (2022) 263.
26. Y.Z. Li, X.P. Guo and G.A. Zhang, *Corros. Sci.*, 123 (2017) 228.
27. E.M. Gutman, *Corros. Sci.*, 49 (2007) 2289.
28. M.M. Hall Jr, *Corros. Sci.*, 51 (2009) 225.
29. T.Q. Wu, J. Xu, M.C. Yan, C. Sun, C.K. Yu and W. Ke, *Corros. Sci.*, 83 (2014) 38.
30. B. Wang, X.B. Li, J. Liu and H. Jiang, *Mater. Corro.*, 69 (2018) 888.
31. Q.J. Meng and G.S. Frankel, *J. Electrochem. Soc.*, 151 (2004) B271.
32. L. Wang, B. Wang, L.Z. Luo, H. Jiang and J. Liu, *Mater. Corro.*, 71 (2020) 1971.
33. M.A. Arshadi, J.B. Johnson and G.C. Wood, *Corros. Sci.*, 23 (1983) 763.
34. Y. Li, *Int. J. Electrochem. Sci.*, 17 (2022) 22014.
35. S. Oesch and M. Faller, *Corros. Sci.*, 39 (1997) 1505.
36. D.B. Blücher, J.E. Svensson and L.G. Johansson, *J. Electrochem. Soc.*, 152 (2005) B397.